A HYBRID VORTEX METHOD FOR FLOWS OVER A BLUFF BODY

M. CHENG, Y. T. CHEW AND S. C. LUO

Department of Mechanical and Production Engineering, National University of Singapore, Singapore 119260, Singapore

SUMMARY

A hybrid vortex method was developed to simulate the two-dimensional viscous incompressible flows over a bluff body numerically. It is based on a combination of the diffusion–vortex method and the vortex-in-cell method by dividing the flow field into two regions. In the region near the body surface the diffusion–vortex method is used to solve the Navier–Stokes equations, while the vortex-in-cell method is used in the exterior domain. Comparison with results obtained by the finite difference method, other vortex methods and experiments shows that the present method is well adapted to calculate two-dimensional external flows at high Reynolds number. It is capable of calculating not only the global characteristics of the separated flow but also the evolution of the fine structure of the flow field with time precisely. The influence of the grid system and region decomposition on the results will also be discussed.

KEY WORDS: bluff body; hybrid vortex method

1. INTRODUCTION

Since the introduction of the vortex calculation method by Rosenhead[1] in 1931, much progress has been made in refining the method for simulating large-scale structures that are complementary to experimental data and to predict flow characteristics which cannot be measured. An excellent review, covering most aspects of discrete vortex methods in great detail, has been written by Sarpkaya.[2]

There are many kinds of vortex method, each with its inherent advantages and disadvantages, but in general all vortex methods are capable of predicting the global features of unsteady separated flow and the flow field far from the vorticity layer at high Reynolds number reasonably. They are also relatively time-saving in computation because the methods are discrete only with respect to vorticity sheets but not with respect to the whole velocity field.

The main feature of the discrete vortex method is that isolated line vortices or vorticity blobs are introduced into the flow field and tracked numerically by a Lagrangian scheme. In this method, by using potential flow theory and the Biot–Savart law to determine the velocity field, one need not use a fixed mesh grid. However, the singular behaviour of the point vortex can lead to a physically impossible flow velocity and instabilities. Moreover, the number of numerical operations is proportional to N^2 (N is the number of point vortices) when the velocity is determined by the Biot–Savart law, and the CPU time increases rapidly with increasing number of point vortices.

The vortex-in-cell method[3] bypasses the Biot–Savart law. In this method a Lagrangian frame is used to track the vortices and a Eulerian frame is used to calculate the velocity field. A fixed mesh grid is required to determine the velocity field. The number of calculations is $M \log_2 M$ (M is the

number of grid points) when the velocity is determined by solving the Poisson equation. An increase in the number of vortices does not lead to a rapid increase in the number of calculations. However, the accuracy of the results depends on the number of grid nodes. A sufficiently fine grid is required to obtain a reasonable result. Also, a pseudoviscosity, which is inherent in the vortex-in-cell method, is introduced into the flow. Some regard the above as an advantage, since the pseudoviscosity stabilizes the velocity field calculations.

In order to simulate viscous diffusion, a random walk method was proposed by Chorin[4] in 1973. With this method the time integration is divided into pure diffusion and inviscid convection by the operator-splitting approach. During time step Δt the pure linear diffusion equation and the inviscid non-linear convection equation are solved separately. The solution of the diffusion equation is simulated stochastically by a 2D displacement of the vortex elements in two orthogonal directions using two independent sets of Gaussian random numbers. The convection velocity is determined by either the Biot–Savart law or the vortex-in-cell method. The random walk method can reflect the diffusion or vorticity. However, since the precision of the method is proportional to $1/\sqrt{N}$ (N is the number of point vortices), the number of vortices must be $O(Re)$ to ensure sufficient precision. Thus, a large amount of computation is required to obtain a good simulation.

A diffusion–vortex method was proposed by Lu and Ross in 1991.[5] In this method, following Chorin, the vorticity transport equation is divided into the linear diffusion equation and the non-linear convection equation. The diffusion process for each time step is simulated by the solution of the diffusion equation instead of by the random walk approximation. The convection velocity at each mesh point is determined by solving the Poisson equation. This method can reduce the total CPU time and avoid cut-off procedures of vortices. However, to obtain a good diffusion simulation accuracy, the constraint condition of grid size must be satisfied. In fact, this method is unsuitable for calculation in the far wake.

Despite the increasing power of computers, any solitary vortex method still suffers difficulties in some situations. In order to overcome the existing problems of vortex methods, some hybrid vortex schemes have been devised. A deterministic hybrid vortex method,[6] which consists of solving the viscous vorticity equation by interlacing a finite difference method for diffusion and a vortex-in-cell method for convection, has been used to study the flow around an impulsively started circular cylinder. It is believed that the hybrid vortex method remains one which requires further research and evaluation.

It is well known that for the case of high-Reynolds-number flow past a bluff body the effects of viscosity are generally limited to the thin boundary layers on the body and the wake behind it. Thus the distribution of vorticity in the flow field is sufficiently compact for its idealization in terms of singularities embedded in an otherwise inviscid domain. The higher the Reynolds number, the more compact is the region of vorticity. At high Reynolds number the whole flow field can be divided into two regions and different methods can be applied to calculate the flow in each region. Some researchers[7,8] have applied the discrete vortex method combined with boundary layer theory to simulate the flow past a circular cylinder. The results showed that the vortex method is both simple and efficient for predicting lift and drag forces that are consistent with the experimental results reported. More recently, in order to further improve the method and to reduce the difficulty in the finite difference solution of the Navier–Stokes equations at high Reynolds number, a domain decomposition hybrid method which combines a vortex method and a finite difference method has been used by some researchers[9,10] to simulate two-dimensional external viscous flows. The results showed that the method has the advantage of the finite difference solution for the Navier–Stokes equations in predicting precisely the fine structure of the flow field, as well as the advantage of the vortex method in computing efficiently the global characteristics of the separated flow. It saves computer time and reduces the amount of computation as compared with pure Navier–Stokes equation solution.

At high Reynolds number the real flow will only remain two-dimensional in the starting flow for a limited time. Recently, the effect of three-dimensionality on the lift and drag forces of nominally two-dimensional cylinders was investigated numerically by Mittal and Balachandar.[11] Their results show that the drag coefficient computed from two-dimensional simulations is higher than that obtained from experiments and the difference between the drag computed from two-dimensional and three-dimensional simulations is very much dependent on the cylinder geometry. Their results also show that the frequencies of the lift and drag coefficients seem unchanged. Three-dimensional simulations of flow lead to accurate prediction of drag, but they remain very expensive and are limited to moderate Reynolds numbers. However, two-dimensional simulations are quite feasible, even for complex geometries and relatively high Reynolds numbers. Thus it is not uncommon to use two-dimensional simulations to predict the aerodynamic characteristics of a wing or the wind loads on a skyscraper.

The purpose of the present paper is to develop a hybrid vortex method for two-dimensional bluff body flows at moderate Reynolds numbers. The method can be considered as a combination of the diffusion–vortex method and the vortex-in-cell method by dividing the flow field into two regions. In the region near the body surface the diffusion–vortex method is used to solve the Navier–Stokes equations. In the exterior domain the vortex-in-cell method is used. In order to illustrate the usefulness and accuracy of the present method, we consider three cases of flow past a circular cylinder. Although the flow around a fixed circular cylinder may remain highly two-dimensional only up to a Reynolds number of 200 owing to the perturbation in real flow, in the present investigation of the flow past a rotating cylinder and rotationally oscillating cylinder the imposed perturbation is two-dimensional and should at least improve the two-dimensionality of our present rather low-*Re* flow. Some comparisons with experiments and numerical simulation are performed.

2. BASIC EQUATION

Let us consider a two-dimensional, viscous and incompressible flow past a circular cylinder with constant velocity $\tilde{U}_\infty$.

The flow is governed by the continuity equation and Navier–Stokes equations as

$$\nabla \cdot \tilde{\mathbf{u}} = 0, \tag{1}$$

$$\frac{\partial \tilde{\mathbf{u}}}{\partial \tilde{t}} + (\tilde{\mathbf{u}} \cdot \nabla)\tilde{\mathbf{u}} = -\frac{1}{\tilde{\rho}} \nabla \tilde{p} + \tilde{v}\nabla^2 \tilde{\mathbf{u}}. \tag{2}$$

The streamfunction $(\tilde{\psi})$ and vorticity $(\tilde{\zeta})$ formulation in dimensionless form can be obtained from (1) and (2) as

$$\frac{\partial \zeta}{\partial t} - \nabla \cdot [\zeta \nabla \times (\psi\mathbf{k})] = \frac{2}{Re}\nabla^2 \zeta, \tag{3}$$

$$\nabla^2 \psi = -\zeta. \tag{4}$$

The relations of streamfunction and vorticity with velocity $\mathbf{u}$ are

$$\mathbf{u} = \nabla \times (\psi\mathbf{k}), \tag{5}$$

$$\zeta\mathbf{k} = \nabla \times \mathbf{u}. \tag{6}$$

Dimensionless variables are defined according to

$$\mathbf{r} = \frac{\tilde{\mathbf{r}}}{\tilde{a}}, \qquad \mathbf{u} = \frac{\tilde{\mathbf{u}}}{\tilde{U}_\infty}, \qquad \psi = \frac{\tilde{\psi}}{\tilde{U}_\infty \tilde{a}}, \qquad \zeta = \frac{\tilde{a}\tilde{\zeta}}{\tilde{U}_\infty}, \qquad t = \frac{\tilde{U}_\infty \tilde{t}}{\tilde{a}}, \qquad Re = \frac{2a\tilde{U}_\infty}{\tilde{v}}, \tag{7}$$

where the superscript tilde denotes the dimensional variables, $\tilde{\mathbf{r}} = \tilde{x}\mathbf{i} + \tilde{y}\mathbf{j}$, $\mathbf{i}, \mathbf{j}$ and $\mathbf{k}$ are unit vectors in the three directions of the right-handed co-ordinate system $(\tilde{x}, \tilde{y}, \tilde{z})$ respectively, $\tilde{v}$ is the kinematic viscosity, $\tilde{t}$ is the time, $\tilde{U}_\infty$ is the velocity at infinity and $\tilde{a}$ is the characteristic dimension of the body; when the body is a circular cylinder, $\tilde{a}$ is the radius of the cylinder.

3. THE HYBRID VORTEX CALCULATION METHOD

3.1. Operator splitting

It is well known that the vorticity transport equation (3) represents the two mechanisms of vorticity diffusion and vorticity convection which occur simultaneously. For high-Reynolds-number flow, in order to simplify the problem and following Chorin,[4] the time integration is divided into two fractional steps: pure diffusion and inviscid convection. Thus during each time step Δt the pure linear diffusion equation

$$\frac{\partial \zeta}{\partial t} = \frac{2}{Re} \nabla^2 \zeta \tag{8}$$

and the inviscid non-linear convection equation

$$\frac{\partial \zeta}{\partial t} = -(\mathbf{u} \cdot \nabla)\zeta \tag{9}$$

are solved separately.

3.2. Domain decomposition

In order to effectively solve equations (8) and (9) by applying the hybrid vortex method, the entire flow field is covered by a net of mesh points and divided into two regions. Region 1 is the 'layer' with the thickness of $O(\delta)$ near the cylinder surface, where δ is the boundary layer thickness on the surface of the cylinder. When the radius of curvature of the body surface is equal to or greater than unity, the thickness of region 1 is estimated by the flat plate boundary layer thickness.[12] Region 2 is the slightly viscous flow region outside the 'layer' and extends from the boundary of the 'layer' to infinity.

3.3. The hybrid vortex algebra

In region 1 the flow is viscous. The vorticity produced at the wall is carried away by convection and diffusion. Flow separation occurs and large deformation of streamlines exist there. These processes determine the entire flow field which in turn controls the production of vorticity. The diffusion–vortex method is used to simulate the unsteady flow field near the wall, since it is not only avoids the difficulties in cut-off properties of the vortices but also reduces the CPU time.

When the diffusion–vortex method is applied, the vorticity field ζ at time $t_0 + \Delta t$ can be determined by solving equation (8) once the vorticity distribution at time t_0 is known. Let us consider the vorticity diffusion equation with the initial distribution $\zeta_0(\mathbf{r}, t_0)$ at time t_0 and given $\zeta_B(t)$ along the boundary:

$$\frac{\partial \zeta}{\partial t} = \frac{2}{Re} \nabla^2 \zeta, \tag{10}$$

$$\zeta|_B = \zeta_B, \tag{11}$$

$$\zeta|_{t=t_0} = \zeta_0. \tag{12}$$

The solution of equations (10)–(12) at time $t_0 + \Delta t$ can be written as[13]

$$\zeta(\mathbf{r}, t_0 + \Delta t) = \iint\limits_{\Omega} G\zeta_0(\mathbf{r}', t_0)\mathrm{d}\Omega - \frac{2}{Re}\int_{t_0}^{t_0+\Delta t} \mathrm{d}\tau \int_s \zeta_{\mathrm{B}} \left.\frac{\partial G}{\partial n}\right|_{\mathrm{B}} \mathrm{d}s, \tag{13}$$

where G is the appropriate Green function, defined by

$$\frac{\partial G}{\partial t} = \frac{2}{Re}\nabla^2 G + \delta(\mathbf{r} - \mathbf{r}')\delta(t - \tau), \tag{14}$$

$$G|_{\mathrm{B}} = 0 \quad (t > \tau), \tag{15}$$

and $(\partial G/\partial n)|_{\mathrm{B}}$ indicates the derivative in the direction normal to the surface B.

Since the influence of the neighbouring vortices falls away exponentially with distance squared, the region of vortex diffusion is very small when $Re \gg 1$. It is thus reasonable that the Green function for a flat plate is used as an approximation as long as $\lambda \ll R$ ($\lambda = \sqrt{(4\Delta t/Re)}$, R being the radius of curvature of the solid surface).[5] For example, for $\Delta t = 0.02$ and $Re = 1000$, $\lambda = 8.944 \times 10^{-3}$, which is indeed much smaller than $R = 1$. When the solution of the flat palte is used as an approximation to the solution of the present problem, the function G in region 1 can be written as

$$G = \frac{1}{4\pi\Delta t\gamma^2}(\mathrm{e}^{-r_1^2/4\Delta t\gamma^2} - \mathrm{e}^{-r_2^2/4\Delta t\gamma^2}), \tag{16}$$

where

$$\gamma^2 = 2/Re, \tag{17}$$

$$r_1^2 = (x - x_1)^2 + (y - y_1)^2, \tag{18}$$

$$r_2^2 = (x - x_2)^2 + (y - y_2)^2, \tag{19}$$

r_1 is the distance between the vortex point at (x_1, y_1) and the calculated point (x, y) and r_2 is the distance between the image vortex point at (x_2, y_2) and the calculated point (x, y).

In region 1 each vortex is diffused during Δt to spread its vorticity in a Gaussian distribution manner to all the mesh points. By summing up all contributions, new vortices are created at the mesh points after each time step Δt. They are then convected according to equation (9). In contrast with the usual Lagrangian vortex methods, these vortices move only one time step. The redistribution of vorticity to the mesh points at each time step can cause numerical diffusion. However, when the mesh length h ($h = \max(\Delta r, r\Delta\theta)$) satisfies the condition $h \leqslant 1.756(\Delta t/Re)^{1/2}$ presented by Lu and Ross,[5] the error generated by the vorticity redistribution is $O(10^{-5})$.

In region 2 the effects of viscosity can be neglected for high-Reynolds-number flow. Therefore the flow far away from the cylinder can be approximated as inviscid potential flow. Thus it can undergo only convection and deformation according to equation (9). The convection of vortices is calculated by using the discrete vortex method and the vortex-in-cell method. Namely, when a vortex with strength Γ reaches its new location, it contributes an incremental vorticity ζ to the four surrounding mesh points according to the area-weighting scheme. The corresponding vorticity distribution on the ith grid nodes is

$$\zeta_i = \frac{A_i}{A^2}\Gamma \quad (i = 1, 2, 3, 4), \tag{20}$$

where A is the grid cell area and A_i is the area diagonally opposite the ith node.

In the present method the interface is similar to a 'vorticity source surface' and vorticity is transferred from region 1 to region 2 by diffusion and convection. There is no additional condition on the interface.

After the vorticity distribution at each mesh point at time t has been calculated, the velocity is determined via the streamfunction by solving the Poisson equation (4) together with appropriate boundary conditions. When the outer boundary is not far from the cylinder, a convective outlet boundary condition of the form $\partial \mathbf{u}/\partial t + c \partial \mathbf{u}/\partial x = 0$ is more appropriate as it minimizes the distortion of the convecting vortices.[14] The potential flow condition is also reasonable when the outer boundary is far from the cylinder. The influence of the computational domain on the wake of a circular cylinder has been studied by Stansby and Slaouti.[15] Their results show that the Strouhal numbers with the computational domain radius $\tilde{r}_\infty/\tilde{a} = 120$ and 400 at $Re = 100$ are very close to that with $\tilde{r}_\infty/\tilde{a} = 200$. They found that neither the proximity of the outer mesh boundary to the cylinder nor the proximity of the wake to the downstream boundary has a significant influence. The influence on forces was similarly insignificant. Furthermore, the same results can be seen from the time evolution of force coefficients reported by some researchers.[16,17] Therefore the influence of vortices crossing the outflow boundary on the vortex structure in the near-wake and forces is small so that it can be ignored as long as $\tilde{r}_\infty/\tilde{a}$ is large enough (the value of $\tilde{r}_\infty/\tilde{a}$ used in our computation is 111).

Here equation (4) will be solved together with the boundary conditions

$$\psi|_{\mathrm{B}} = \psi_{\mathrm{B}}, \tag{21}$$

$$\nabla \times (\psi \mathbf{k})|_\infty \to \mathbf{u}_\infty \tag{22}$$

by a subroutine (FPS2H) for all numerical examples. The subroutine, available from the IMSL mathematical package, for solving the Poisson equation is based on representing the elliptic equation in finite difference form using a method developed by Lynch and Rice[18] and known as the HODIE (high-order difference approximation with identity expansion) method. The resulting system of linear algebraic equations is solved using fast Fourier transform techniques.[19]

According to equation (9), the vortex at each mesh point after a time interval Δt is displaced to the location

$$\mathbf{r}(t + \Delta t) = \mathbf{r}(t) + \tfrac{1}{2}[3\mathbf{u}(t) - \mathbf{u}(t - \Delta t)]\Delta t, \tag{23}$$

which is a second-order-accurate integration scheme.

On the other hand, the vorticity boundary condition is determined from the Poisson equation (4). In this paper a second formula is proposed that can be written as

$$\zeta|_{\mathrm{B}} = -\frac{6[\psi(\Delta, t) + u_{\mathrm{B}}\Delta] + \zeta(\Delta, t)\Delta^2}{2\Delta^2}, \tag{24}$$

where $\Delta = -\mathbf{n} \cdot d\mathbf{r}$, $\mathbf{n}$ is the inward-to-body normal vector and u_{B} is the surface velocity of the body.

After the vorticity has been distributed to replace the initial vorticity field, the procedure of calculation is repeated until the time duration of interest is covered.

4. NUMERICAL EXAMPLES AND COMPARISONS

4.1. Influence of calculation parameters

In order to discuss the influence of the grid system, region decomposition and time step on the results, we consider the case of flow past a circular cylinder. It is convenient to use the polar co-ordinate system (r, θ) and introduce the transformation $\xi = \ln r$. Here the total computational domain has been limited to $\xi_\infty = 3\pi/2$ ($\tilde{r}_\infty/\tilde{a} \approx 111$). Since the diffusion equation is being solved in region

1, it is necessary to know the initial vorticity distribution. The vorticity is initially confined to an infinitesimally thin region surrounding the cylinder surface. The initial vorticity can be approximated from Rayleigh's solution as

$$\zeta = -\sqrt{\left(\frac{Re}{2t\pi}\right)}(2\sin\theta + u_{\mathrm{B}})\mathrm{e}^{-(Re/8t)(\mathrm{e}^{\xi}-1)^2} \quad (t \to 0). \tag{25}$$

The calculation for the test problems starts at $t = 0.001$ using equation (25).

Three grid systems, three sizes of region 1 and two time steps were considered for flow at Reynolds number equal to 3000. A comparison of the streamline patterns at $t = 5$ was made between the present results and the flow visualization result of Bouard and Coutanceau[20] as shown in Figure 1. It should be noted from the results shown in Figure 1 that when the number of grid nodes increases from $I \times J = 129 \times 257$ to $I \times J = 257 \times 513$ (where I and J are the numbers of grid points in the directions ξ and θ respectively, $\Delta\xi = \xi_{\infty}/I$ and $\Delta\theta = 2\pi/J$), the calculated streamline pattern agrees better with the experimental results.[20] The grid $I \times J = 257 \times 513$ is satisfactory in the comparison of global streamline patterns, though the secondary vortices are slightly larger for the finer grid $I \times J = 513 \times 513$. On the other hand, when the grid increases from $I \times J = 257 \times 513$ to $I \times J = 513 \times 513$, the CPU time for each time step increases by about 150%.

The influence of the number of grid nodes, size of region 1 and size of time step is checked for the drag coefficient C_{D} ((drag force)/$\tilde{\rho}\tilde{U}_{\infty}^2\tilde{a}$, where $\tilde{\rho}$ is the fluid density) in Figure 2. The drag coefficient as shown in Figure 2(a) increases when the number of grid nodes increases. When the number of nodes increases from $I \times J = 129 \times 257$ to $I \times J = 257 \times 513$, the mean value of the drag coefficient increases by about 6%. When the number of nodes further increases from $I \times J = 257 \times 513$ to $I \times J = 513 \times 513$, the drag coefficient only increases by less than 2%. Furthermore, it is found that the fluctuation amplitude of the lift and drag coefficients increases slightly with increasing number of grid nodes after the shedding mechanism is initiated. Figure 2(b) shows that the drag coefficient decreases when the size of region 1 increases, but the change is very small. When region 1 increases from $0 \leqslant \xi \leqslant 0.2$ to $0 \leqslant \xi \leqslant 0.8$, the mean value of the drag coefficient
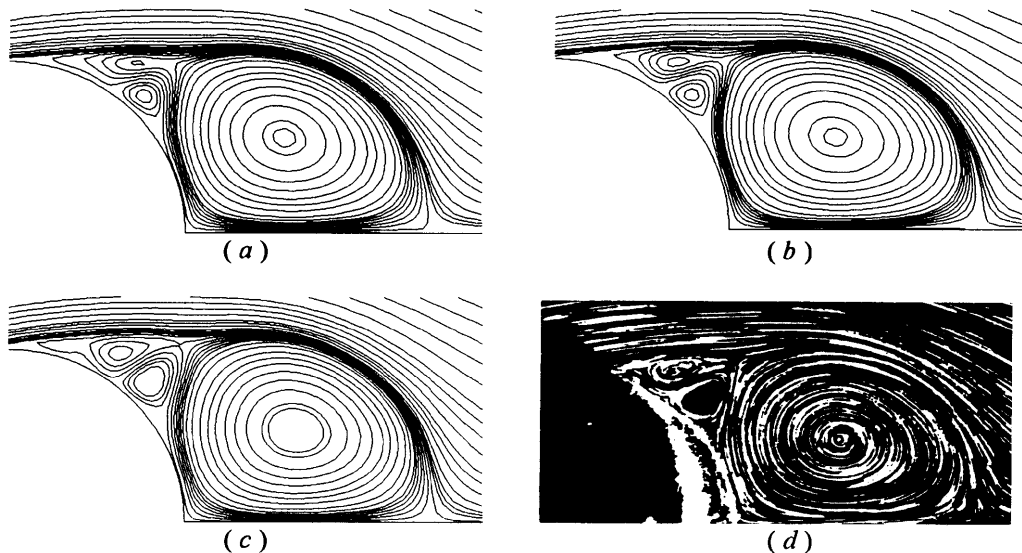
Figure 1. Comparison of streamline patterns for $Re = 3000$ at $t = 5$: (a) present method, $I \times J = 129 \times 257$; (b) present method, $I \times J = 257 \times 513$; (c) present method, $I \times J = 513 \times 513$; (c) flow visualization by Bouard and Coutanceau[20]
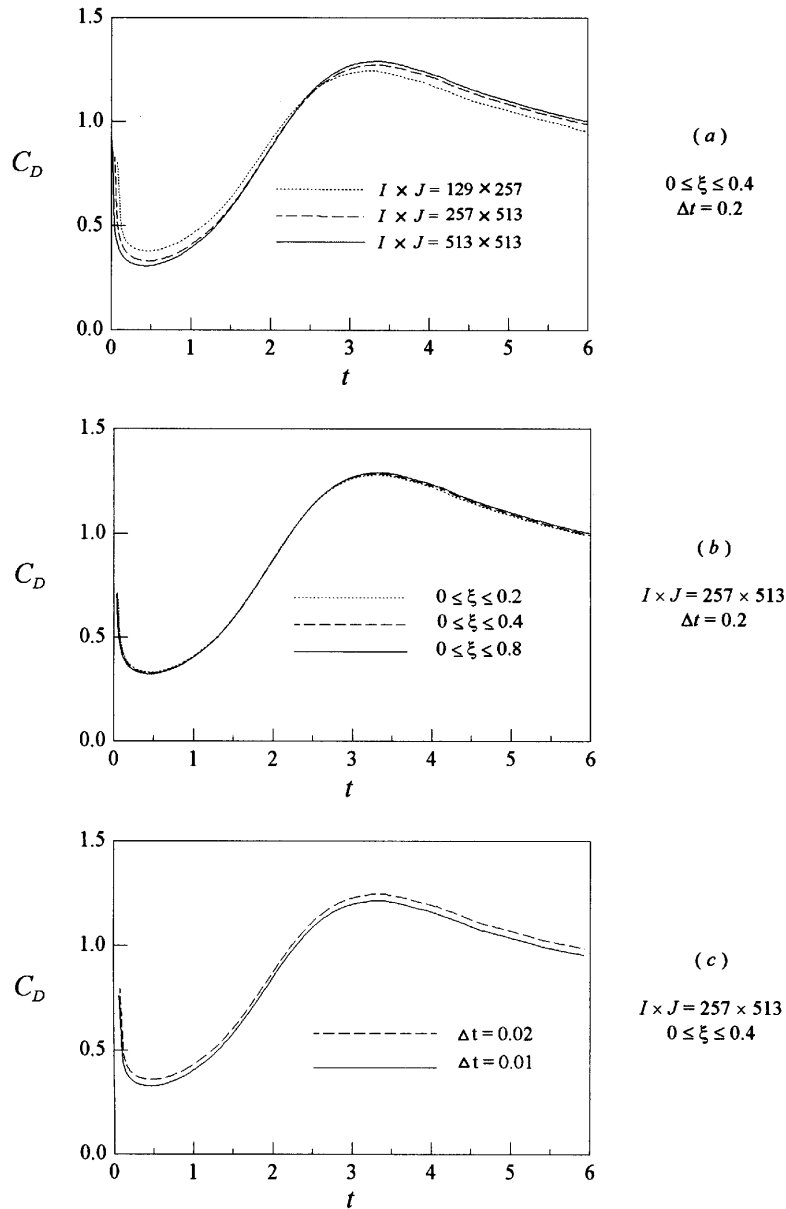
Figure 2. Influence of calculation parameters on drag coefficient for $Re = 3000$: (a) number of grid nodes; (b) size of region 1; (c) size of time step

decreases by less than 2%. Figure 2(c) shows that when the time step increases from 0·01 to 0·02, the drag coefficient increases slightly.

The influence of the size of time step and number of grid nodes is also checked for the radial velocity on the symmetry axis behind the cylinder as shown in Figure 3. It can be seen in Figure 3(a) that no significant difference in the velocity is observed between $\Delta t = 0·01$ and 0·02. The influence of the cylinder of grid nodes on the radial velocity on the symmetry axis behind the cylinder as shown
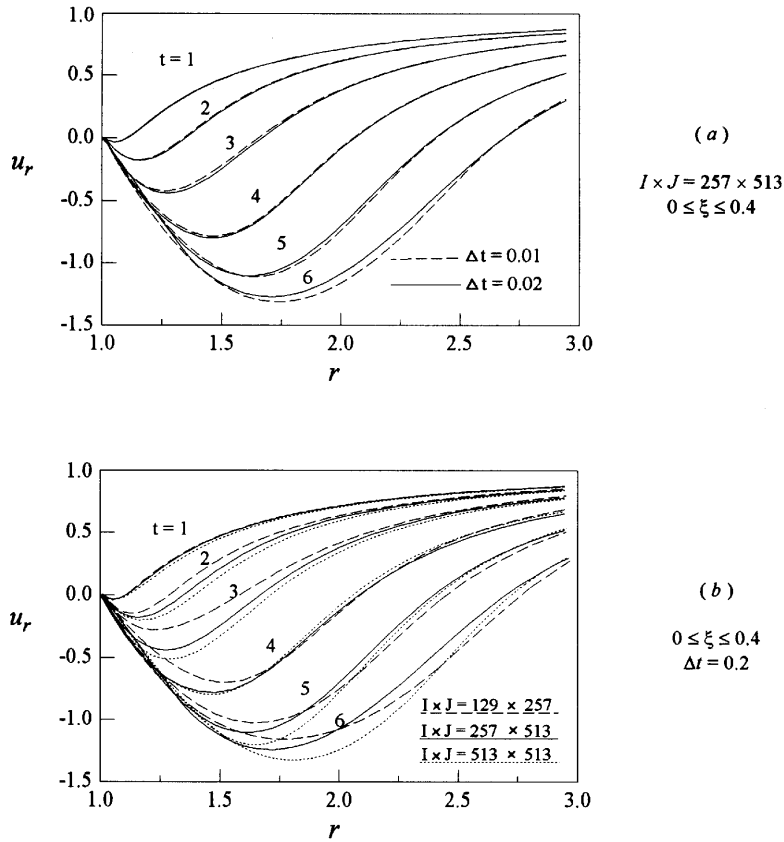
Figure 3. Influence of calculation parameters on radial velocity on symmetry axis behind cylinder for $Re = 3000$: (a) size of time step; (b) number of grid nodes

in Figure 3(b) seems to be slightly larger in the range $r < 2$. It is clearly seen that the difference between the radial velocity distributions for $I \times J = 257 \times 513$ and $I \times J = 513 \times 513$ is smaller than that for $I \times J = 129 \times 257$ and $I \times J = 257 \times 513$.

With the present method, vorticity is recreated at every time step on the vortex-in-cell mesh in region 2. This leads to numerical viscosity when a grid stretched in the radial direction is used. This numerical viscosity does not have any significant effect on the mean drag and flow structure in the near wake, but it does influence the flow structure in the far wake.[21] The effect of numerical viscosity can be reduced by adopting a finer grid system.

All things considered, it is found that if one is interested only in global properties such as force coefficients and Strouhal number, a relatively coarse grid should be adopted. Hence, if the resolution of local properties is also of interest, a finer grid system will be necessary.

In order to further illustrate the usefulness and accuracy of the present method, we consider three cases of flow past a circular cylinder. Taking both calculation time and accuracy into consideration, we had decided on the following. Region 1 corresponds to $0 \leqslant \xi \leqslant 0.4$ and region 2 corresponds to $0.4 \leqslant \xi \leqslant \xi_{\infty}$. A grid of $I \times J = 257 \times 513$ ($\Delta \xi \approx 0.0183$, $\Delta \theta \approx 0.0122$, $0.0185 \leqslant \Delta \tilde{r}/\tilde{a} \leqslant 2$) nodes is

Present   Bouard & Coutanceau (1980) [20]

$(a) t = 1$

$(b) t = 2$

$(c) t = 3$

$(d) t = 4$

$(e) t = 5$
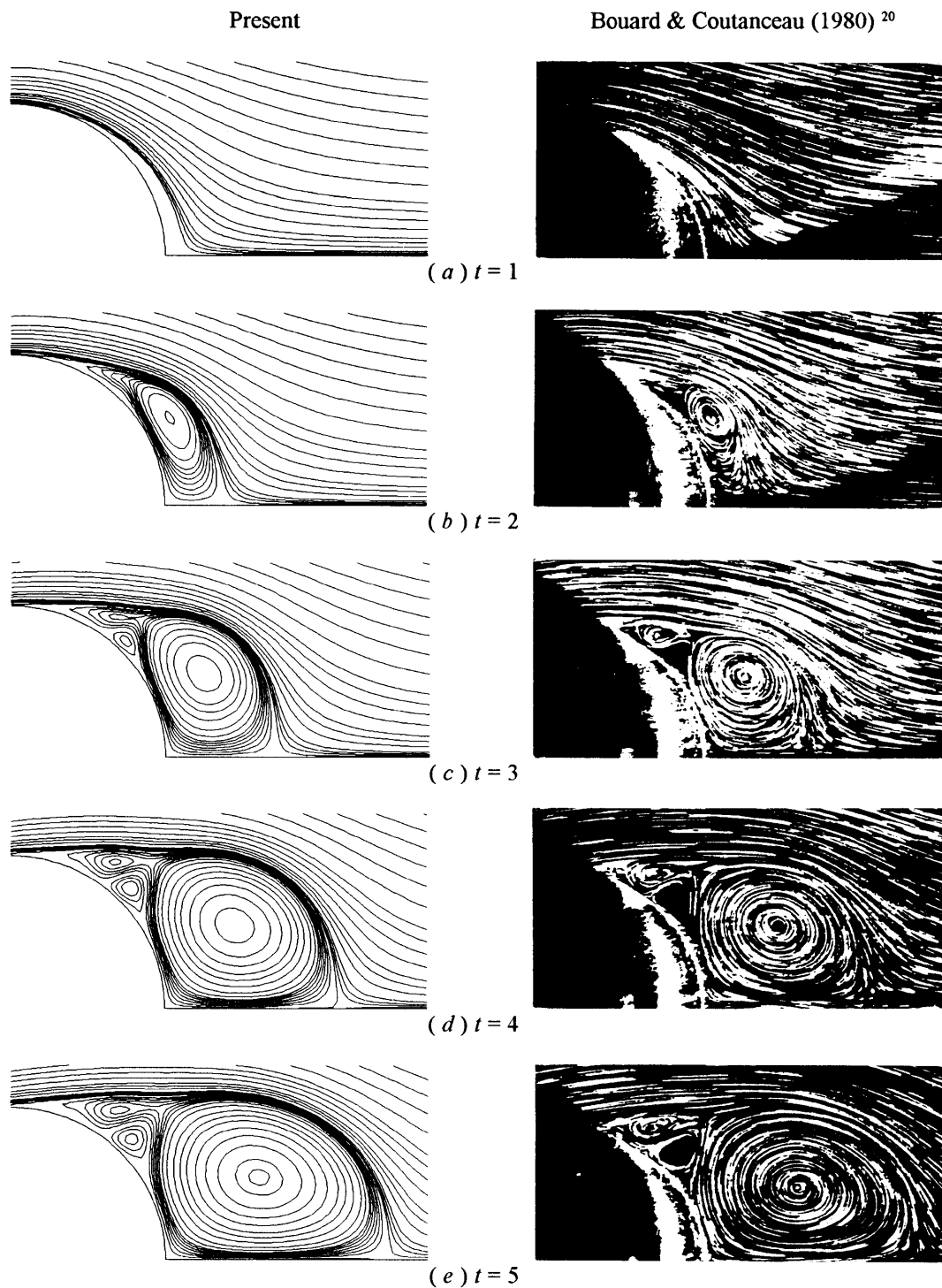
Figure 4. Comparison of experimental flow visualization of Bouard and Coutanceau[20] with streamlines from present numerical calculation for $u_B = 0$ and $Re = 3000$ at times (a) $t = 1$, (b) $t = 2$, (c) $t = 3$, (d) $t = 4$ and (e) $t = 5$

Present   Bouard & Coutanceau (1980) [20]

$(a) t = 1.5$

$(b) t = 2$

$(c) t = 2.5$

$(d) t = 3$
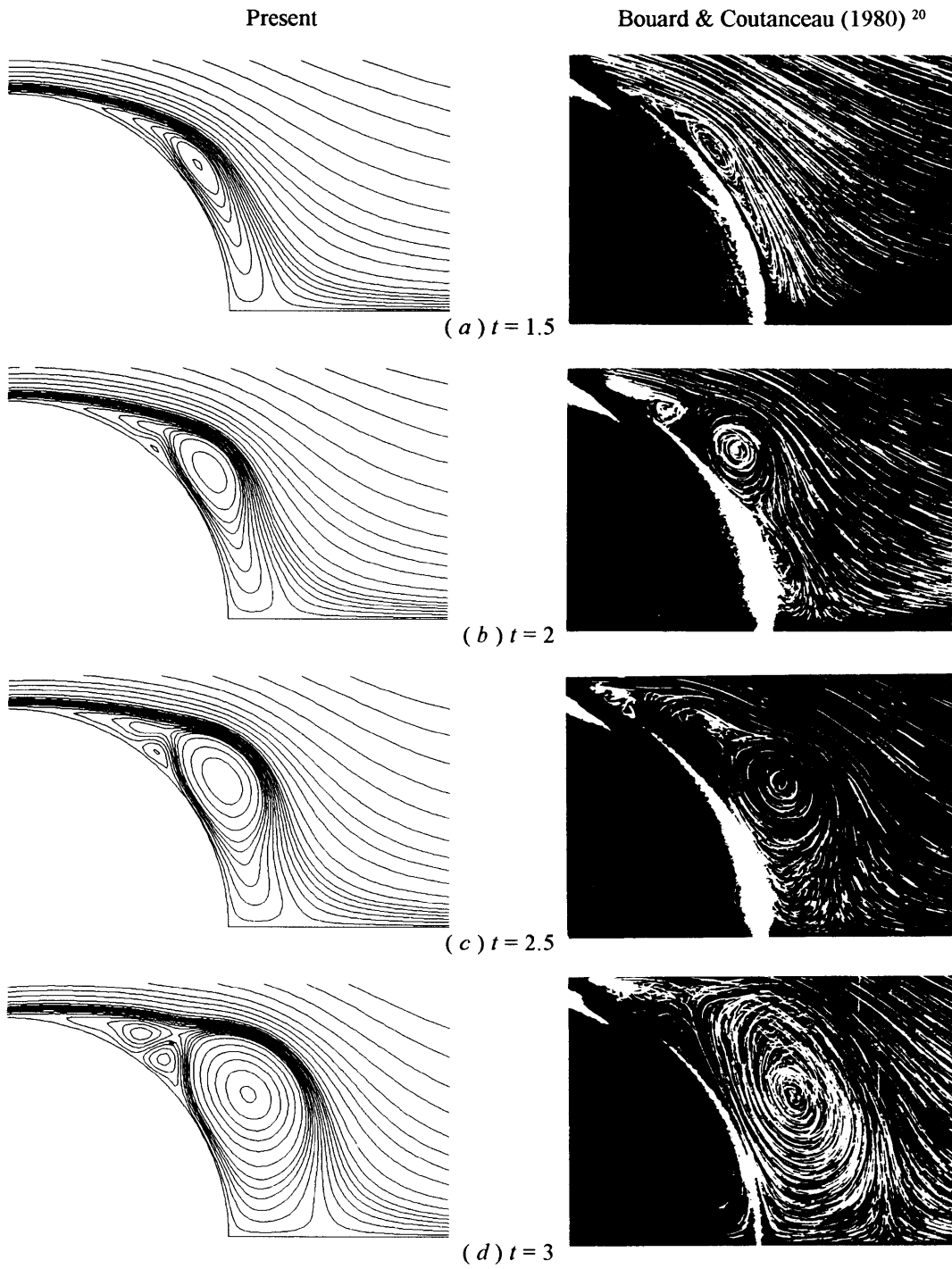
Figure 5. Comparison of experimental flow visualization of Bouard and Coutanceau[20] with streamlines from present numerical calculation for $u_B = 0$ and $Re = 9500$ at times (a) $t = 1.5$, (b) $t = 2$, (c) $t = 2.5$ and (d) $t = 3$

adopted as the basic grid for the entire flow field. The non-dimensional time step is chosen as $\Delta t = 0.02$. The numerical calculations have been made on an IBM 3090 mainframe computer. The CPU time for each time step is equal to about 2 s.

4.2. Flow around an impulsively started circular cylinder

In this case, $u_B = 0$ and $\psi_B = 0$. The initial development of impulsively started flow around a cylinder for $Re = 1000$, 3000 and 9500 has been studied numerically and experimentally by some researchers. A comparison of the streamline patterns with the numerical results of Chang and Chern[6] for $Re = 1000$ was made by us in Reference 21. It shows that generally the agreement between the results obtained by the two methods is good. Comparisons of the streamline patterns with the experimental results of Bouard and Coutanceau[20] for $Re = 3000$ and 9500 are given in Figures 4 and 5 respectively. Since the flow is symmetrical about the line $\theta = 0°$ in these figures, for brevity, only one part of each flow will be shown.

It can be shown from Figure 4 that the present results are in agreement with those obtained by the flow visualization experiment. Both show the elongation with time of the main vortex and the appearance of a secondary vortex of opposite vorticity near the separation point at time $t = 3$. The secondary vortex grows in size until it touches the boundary of the main recirculation zone and splits the main vortex into two parts. Two secondary vortices of opposite vorticity emerge in the part near the separation location and constitute the so-called α-phenomenon at $t > 3$. For $Re = 9500$ the computed results are compared with the experimental flow visualization in Figure 5 for $t = 1.5, 2, 2.5$ and 3. It is seen that the agreement between the experimental flow visualization results and the present calculated results is good.

The qualitative agreement in streamline patterns can be quantified by comparing their main vortex length. It is found that in the case of $Re = 1000$ the values of the dimensionless main vortex length $L = \tilde{L}/\tilde{a}$ (defined in inset of Figure 6) at $t = 1, 2, 3$ and 6 are 0.22, 0.5, 0.8 and 1.8 respectively, at $Re = 3000$ the values at $t = 1, 2, 3, 4$ and 5 are 0.1, 0.32, 0.65, 1.08 and 1.5 respectively and at $Re = 9500$ the values at $t = 1.5, 2, 2.5$ and 3 are 0.12, 0.25, 0.3 and 0.45 respectively. The main vortex length has been plotted as a function of time in Figure 6. For $Re = 1000$ and 3000 the main vortex length increases almost linearly. The figure also shows the results from other studies.[6,20] The results from both numerical methods and the experiments show good agreement.
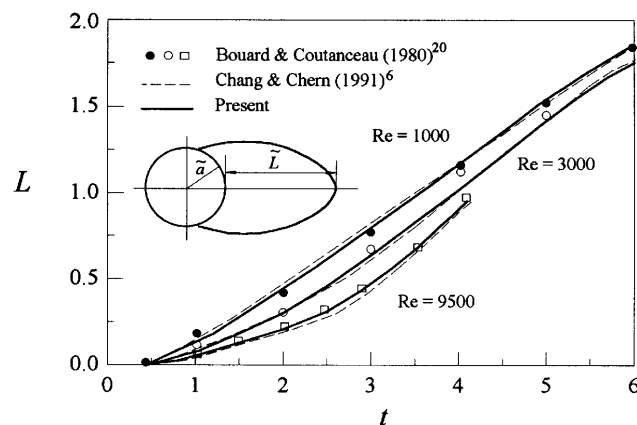
Figure 6. Evolution with time of main vortex length

Figure 7 shows the time evolution of the separation angle θ (defined in inset of Figure 7) for $Re = 1000$. The separation angle increases rapidly and tends towards a stationary value in the early stage of the flow. Comparisons are made with results from other numerical calculations[6,22,23] and again the agreement is good.

Figure 8 gives the radial velocity profiles at $\theta = 0°$. The evolution with time of the radial velocity is compared with the numerical results of Ta[24] at $Re = 1000$ and the experimental results of Bouard and Coutanceau[20] at $Re = 3000$ and 9500. The present results as shown in Figure 8 are in good agreement with the other numerical and experimental results.

Figures 9 and 10 present the evolution with time of the distribution of vorticity at the cylinder surface. A comparison of the time evolution of vorticity distribution over the surface of the cylinder with the analytical results of Bar-Lev and Yang[25] and Collins and Dennis[22] has been conducted for $Re = 1000$. It is found that the present results are also in good agreement with their results during the early stage of the flow. The results in Figure 10 permit the determination of the moment of appearance of a secondary vortex, which is at about $t = 3$, 2·5 and 1·8 when $Re = 1000$, 3000 and 9500 respectively.

A comparison of the time evolution of drag coefficient from the present method and the numerical method of Chang and Chern[6] is given in Figure 11. The agreement of the results generated by the two different numerical methods is good over the range of time investigated.

The time histories of the total lift and drag coefficients C_L ((lift force)$/\tilde{\rho}\tilde{U}_\infty^2\tilde{a}$) and C_D at $Re = 1000$ are shown in Figure 12. In the case of numerical calculations of such a flow there are no destabilizing effects except for the numerical errors. Since the geometry of the flow domain and the boundary conditions are symmetrical, the solution of the equations is also symmetrical. This happens in the present case. Therefore an initial perturbation of the wake is required in order to initiate the alternate vortex shedding. In the present study a rotation of the cylinder is imposed for a short duration to provide the initial perturbation. After a period of evolution the lift and drag coefficients show regular fluctuation with a constant amplitude at $t > 25$ as shown in Figure 12. The ensemble mean fluctuation amplitude of the lift coefficient, $\bar{C}_{Lmax}$, is 1·1. This is higher than the value of $\bar{C}_{Lmax} \approx 0.8$ reported by Ling et al.[9] and is in close agreement with the value of $\bar{C}_{Lmax} \approx 1.05$ reported by Tabata and Fujima,[26] both also at the same Reynolds number of 1000. Stansby and Slaouti[15] reported values of $\bar{C}_{Lmax} \approx 0.3$ and 0·6 at $Re = 60$ and 180 respectively in their computation. The present result at $Re = 1000$ is along the correct trend that $\bar{C}_{Lmax}$ increases with increasing Reynolds number according to available computed results in the literature. Based on the time variations in the lift coefficient, one can determine the Strouhal number of the flow by taking the inverse of the average period of the last five full cycles of oscillation. In the present investigation the
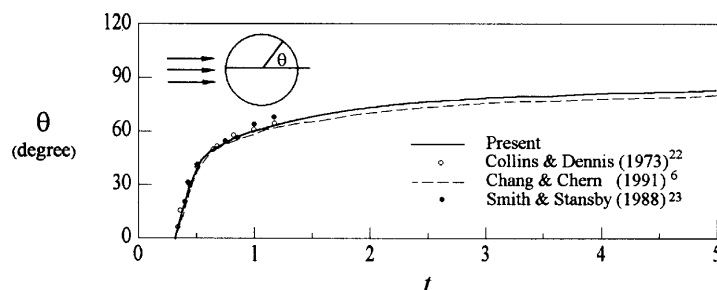
Figure 7. Time variation in separation angle for $Re = 1000$
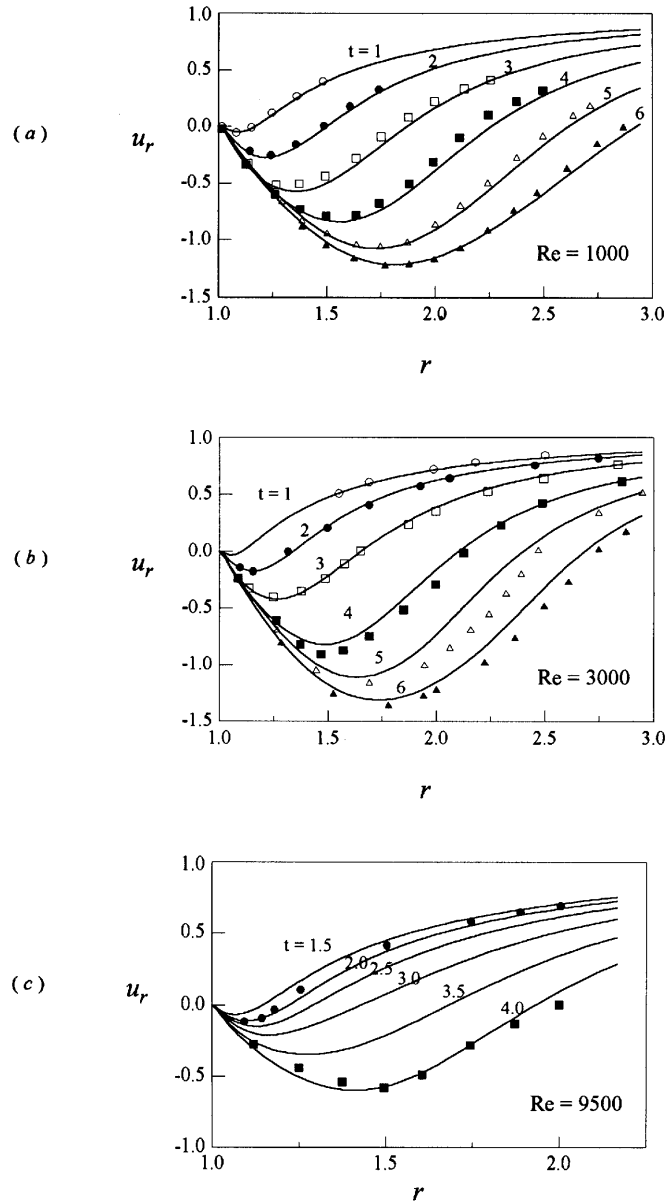
Figure 8. Evolution with time of radial velocity u_r versus r at $\theta = 0°$ for (a) $Re = 1000$ (discrete data taken from Reference 24), (b) $Re = 3000$ and (c) $Re = 9500$ (discrete data taken from Reference 20)

dimensionless vortex-shedding frequency f is equal to 0·103, where $f = 1/T$ and T is the dimensionless period of vortex shedding. The Strouhal number St is related to f by $St = 2f$; St is thus equal to 0·206 for the present case. At $Re = 1000$ the value of St obtained by Roshko[27] in his experiment is about 0·21. This indicates that the vortex-shedding frequency obtained from two-dimensional numerical simulation is agreement with the result obtained from experiment.
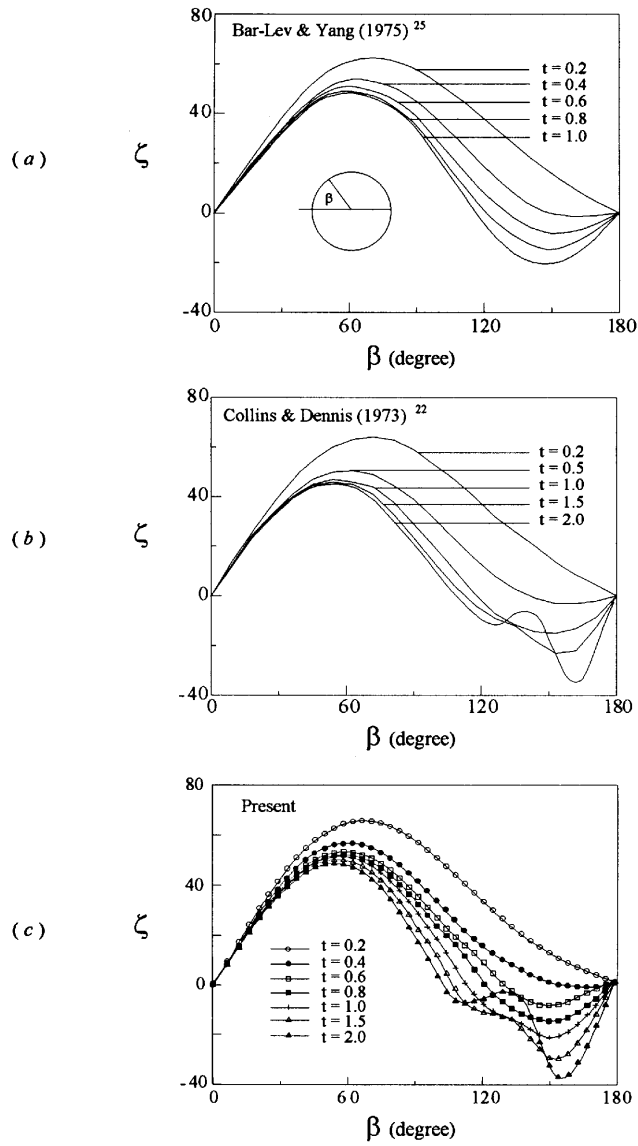
Figure 9. Comparison of time evolution of vorticity distribution over surface of cylinder for $Re = 1000$: (a) Reference 25; (b) Reference 22; (c) Present

4.3. Flow past a rotating circular cylinder

In this case, $u_B = 0.5$ and $\psi_B = 0$. The patterns of instantaneous streamlines for $Re = 1000$ at different times are shown in Figure 13 as extracted from Reference 21. In Figure 13 the present results are shown alongside the experimental results of Badr et al.[28] for $Re = 1000$. At $t = 3$ a secondary vortex appears near the cylinder in the neighbourhood of the second (bottom right) vortex and this secondary vortex is still present at $t = 4$ as shown in Figure 13(b). It should be noted that for the results shown in Figure 13, unlike the non-rotating cylinder case, an artificial initial perturbation
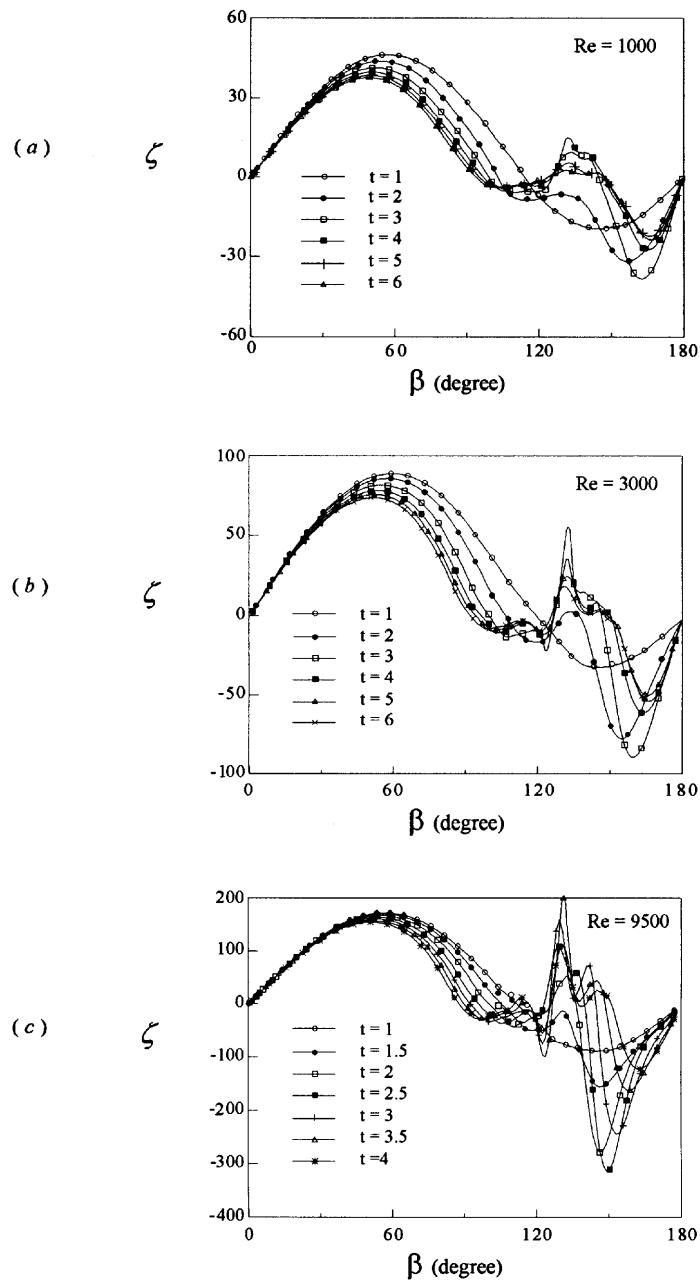
Figure 10. Time evolution of surface vorticity for (a) $Re = 1000$, (b) 3000 and (c) 9500

was not necessary, as the rotation automatically creates asymmetry in the formation of wake flow
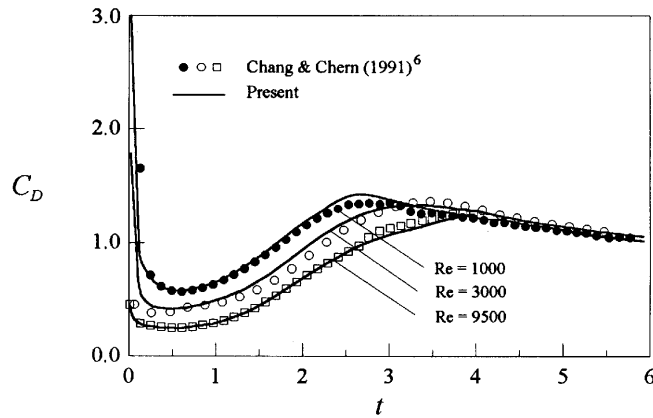
Figure 11. Comparison of time evolution of drag coefficient from two numerical methods for $Re = 1000$, 3000 and 9500

behind the cylinder. Detailed comparisons between experimental and computational results were made by Chew et al.[21] for different u_B. All the comparisons show generally close agreement.

To demonstrate the validity of the present numerical results, some of the present results on initial velocity profiles are compared with the experimental as well as the numerical results[28] at $u_B = 0.5$. The present results shown in Figure 14(a) (extracted from Reference 21) for the radial velocity at $\theta = 0°$ are in better agreement with Badr et al.'s[28] experimental data than are their own computed results. They also indicate quantitatively the growth in attached vortices with increasing t and the approach of velocity towards the freestream value with increasing r. The radial velocity at $\theta = 90°$ in Figure 14(b) (extracted from Reference 21) indicates that the strong shear region caused by cylinder rotation is limited to about 20% of the radial distance from the wall.

In order to check the influence of the initial velocity condition on the result, the variation in the drag coefficient with time using different initial vorticity conditions is shown in Figure 15. It can be seen that the difference in the drag coefficient curves obtained respectively by means of the asymptotic initial vorticity condition as adopted by Chew et al.[21] and Rayleigh's solution as adopted here becomes small as time increases. The difference resulting from the different initial vorticity conditions, as shown in Figure 15, is confined to a very limited time close to $t = 0$. This means that the influence of the initial flow field is small and requires no special treatment in the present method.

Figure 16 shows the time histories of the lift and drag coefficients. It is found that the drag has a dual-periodic behaviour corresponding to the shedding of two different size vortices from the upper and lower sides of the cylinder. The lift shows a periodic behaviour and remains negative for almost the entire run. The same characteristic shapes of lift and drag were reported by Badr et al.[28]
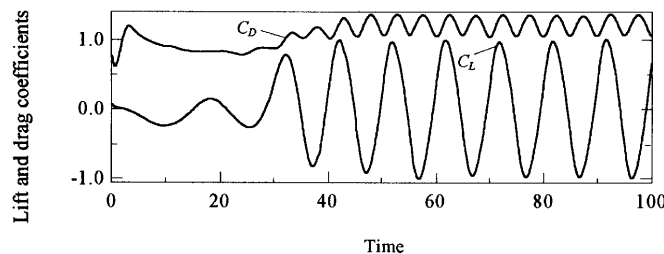
Figure 12. Variation in lift and drag coefficients with time for $u_B = 0$ and $Re = 1000$

Present   **Badr *et al* (1990)** [28]

(*a*) *t* = 3

(*b*) *t* = 4
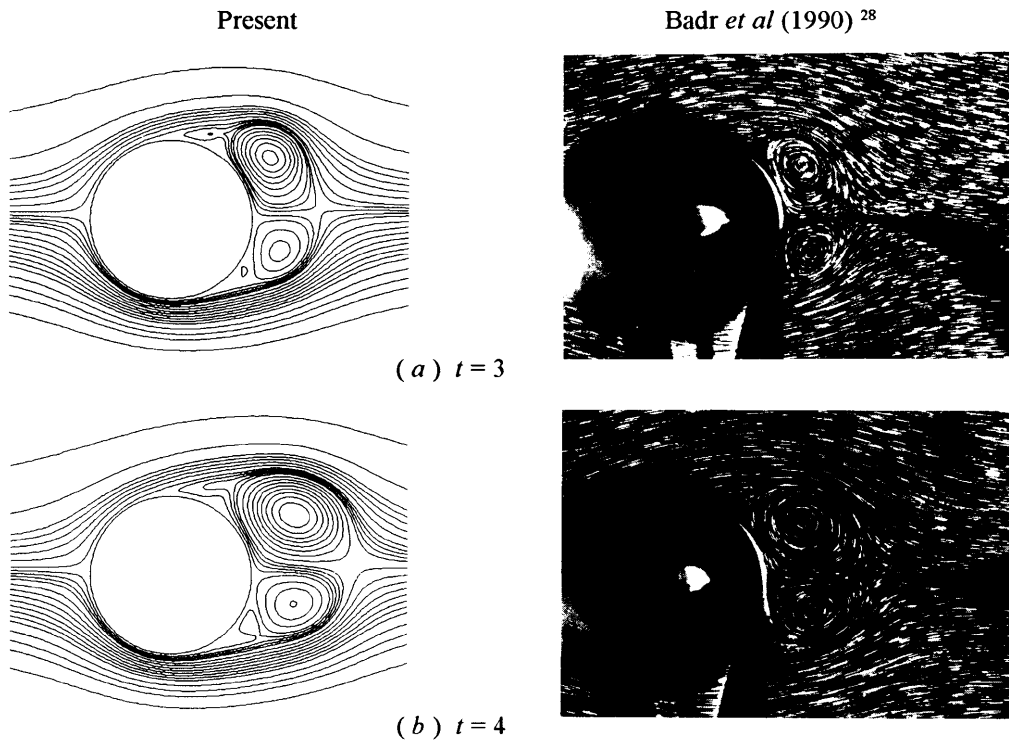
Figure 13. Comparison of streamline patterns with experimental flow visualization for $u_B = 0.5$ and $Re = 1000$ at times (a) $t = 3$ and (b) $t = 4$

(*a*)   (*b*)
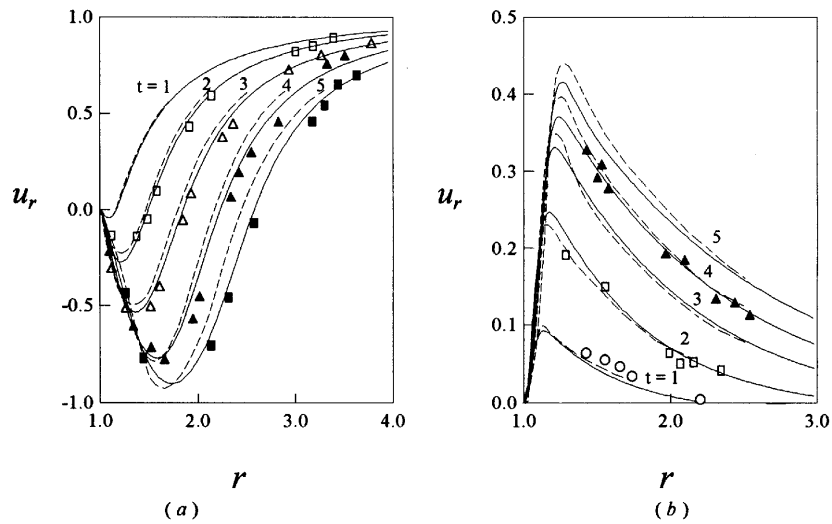
Figure 14. Comparison of velocity profiles for $u_B = 0.5$ and $Re = 1000$: u_r versus r at (a) $\theta = 0°$ and (b) $\theta = 90°$; present calculation, —; Badr *et al.*'s calculation,[28] – – –; experimental points taken from Reference 28
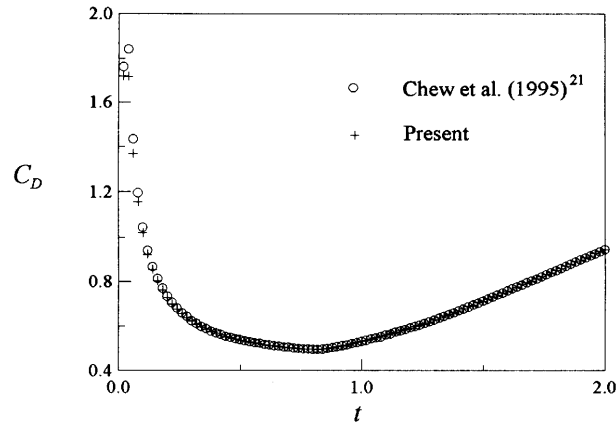
Figure 15. Influence of difference initial vorticity distributions on drag coefficient for $u_B = 0.5$ and $Re = 1000$: o, asymptotic formula as adopted by Chew et al.;[21] +, Rayleigh solution
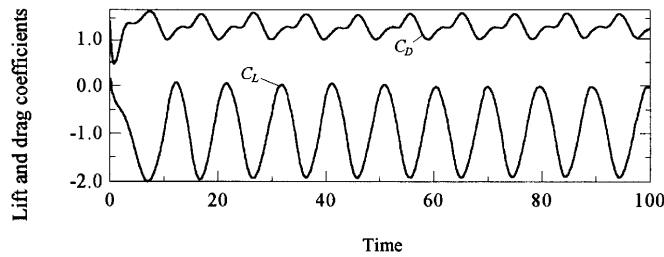
Figure 16. Variation in lift and drag coefficients with time for $u_B = 0.5$ and $Re = 1000$

4.4. Flow around a circular cylinder with rotational oscillations

In this case, $u_B = 3\sin(2\pi f_c t), f_c = 0.5$ and $\psi_B = 0$. Figure 17 shows the streakline patterns of vortex shedding. The phenomenon of vortex–vortex interaction appears clearly in the wake. The details of the merging of small-scale vortices into large-scale vortices are shown chronologically in Figure 17. The visualization experiments by Ongoren and Rockwell[29] and Tokumaru and Dimotakis[30] also show that over a wide range of f_c the perturbed near wake rapidly recovers to a large-scale antisymmetrical pattern similar in form to the von Kármán vortex street.

Figure 18 shows the time histories of the lift and drag coefficient. There are two dominating frequencies in the lift: one of them is the forcing frequency; the other, lower one is the frequency of large-scale vortex formation. The results indicate that the present hybrid method has good stability and adaptability to moving wall boundary conditions.

5. CONCLUDING REMARKS

The numerical results show that the present method is capable of satisfactorily predicting the flow characteristics in the vicinity of a cylinder surface, such as flow separation, surface vorticity distribution, radial and tangential velocity variation, main vortex length and α-phenomenon, as well as the global flow features, such as periodic variations in the flow, lift and drag forces, vortex shedding and Strouhal number. Whenever comparison is possible, the results of the present

(a)

(b)

(c)

(d)

(e)
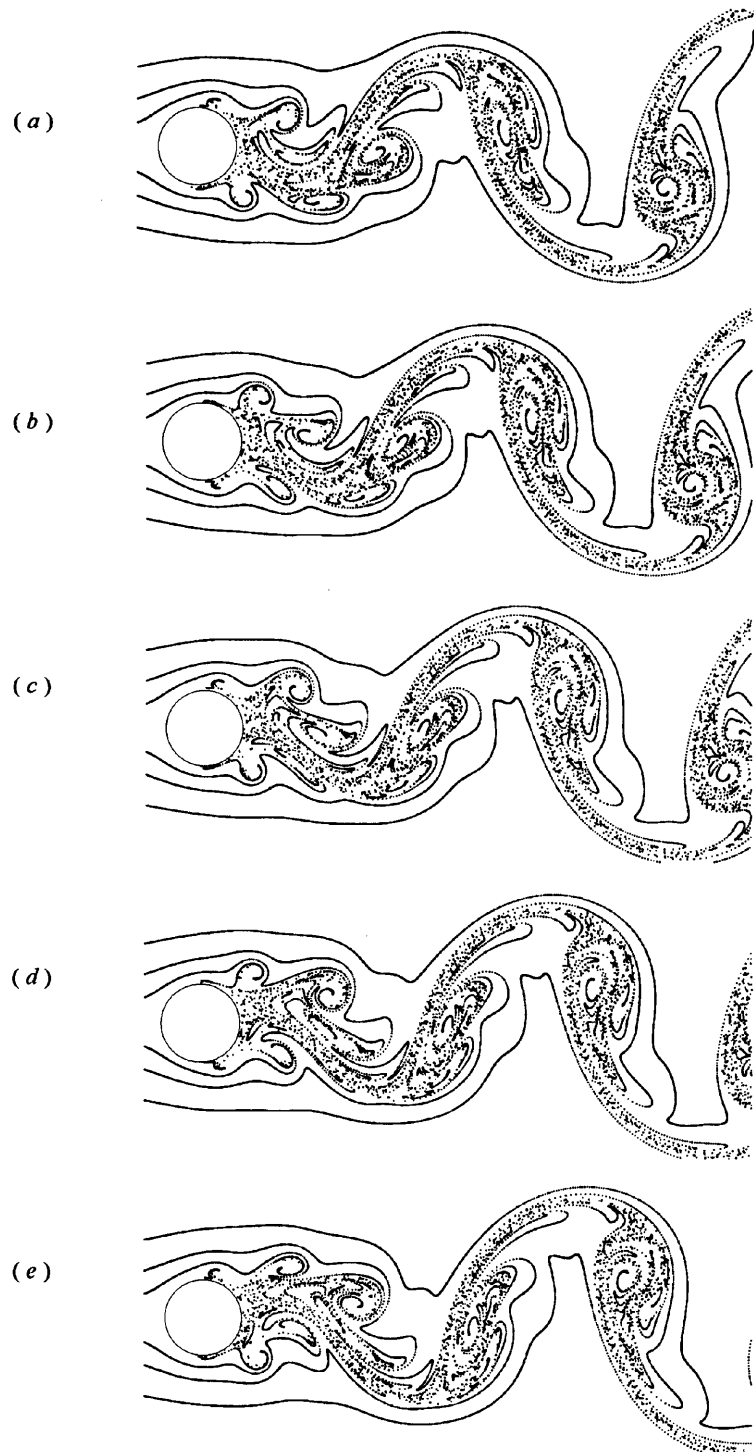
Figure 17. Patterns of streaklines for $u_B = 3\sin(2\pi f_c t)$ and $Re = 1000$ at times (a) $t = 51$, (b) $t = 52$, (c) $t = 53$, (d) $t = 54$ and (e) $t = 55$
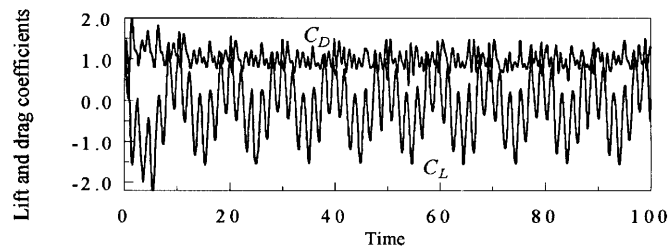
Figure 18. Variation in lift and drag coefficients with time for $u_B = 3\sin(2\pi f_c t)$ and $Re = 1000$

computations are found to be in good agreement with the experimental and numerical results obtained by other investigators. The present method has good stability, simplicity and adaptability to moving wall boundary conditions. More detailed investigations of the flow around bluff bodies at different Reynolds numbers are being carried out by the authors using the hybrid vortex method in further work.

REFERENCES

1. L. Rosenhead, 'The formation of vortices from a surface of discontinuity', *Proc. R. Soc. A*, **134**, 170–192 (1931).
2. T. Sarpkaya, 'Computational methods with vortices—the 1988 Freeman scholar lecture', *J. Fluids Eng.*, **111**, 5–52 (1989).
3. J. P. Christiansen, 'Numerical simulation of hydromechanics by the method of point vortices', *J. Comput. Phys.*, **13**, 363–379 (1973).
4. A. J. Chorin, 'Numerical study of slightly viscous flow', *J. Fluid Mech.*, **57**, 785–796 (1973).
5. Z. Y. Lu and T. Ross, 'Diffusing-vortex numerical scheme for solving incompressible Navier–Stokes equation', *J. Comput. Phys.*, **95**, 400–435 (1991).
6. C. C. Chang and R. L. Chern, 'A numerical study of flow around an impulsively started circular cylinder by a deterministic vortex method', *J. Fluid Mech.*, **233**, 243–263 (1991).
7. T. Kimura and M. Tsutahara, 'Flows about a rotating circular cylinder by the discrete-vortex method', *AIAA J.*, **25**, 182–184 (1987).
8. M. Cheng, Y. T. Chew and S. C. Luo, 'Discrete vortex simulation of the separated flow around a rotating circular cylinder at high Reynolds number', *Finite elem. Anal. Des.*, **18**, 225–236 (1994).
9. G. C. Ling, G. P. Ling and Y. P. Wang, 'Domain decomposition hybrid method for numerical simulation of bluff body flows—theoretical model and application', *Sci. China A*, **35**, 977–990 (1992).
10. J. L. Guermond, S. Huberson and W. Z. Shen, 'Simulation of 2D external viscous flows by means of a domain decomposition method', *J. Comput. Phys.* **108**, 343–352 (1993).
11. R. Mittal and S. Balachandar, 'Effect of three-dimensionality on the lift and drag of nominally two-dimensional cylinders', *Phys. Fluids*, **7**, 1841–1865 (1995).
12. H. Schlichting, *Boundary Layer Theory*, McGraw-Hill, New York, 1968.
13. G. Barton, *Elements of Green's Functions and Propagation Potentials, Diffusion and Waves*, Clarendon, Oxford, 1989.
14. L. L. Pauley, P. Moin and W. C. Reynolds, 'The structure of two-dimensional separation', *J. Fluid Mech.*, **220**, 397–411 (1990).
15. P. K. Stansby and A. Slaouti, 'Simulation of vortex shedding including blockage by the random-vortex and other methods', *Int. j. number methods fluids*, **17**, 1003–1013 (1993).
16. M. Rosenfield, 'Grid refinement test of time-periodic flows over bluff bodies', *Comput. Fluids*, **23**, 693–709 (1994).
17. Y. Lecointe and J. Piquet, 'Computation of unsteady, laminar incompressible, viscous flows using the vorticity streamfunction formulation', in T. K. S. Murthy and C. A. Brebbia (eds), *Computational Methods in Viscous Aerodynamics*, Elsevier, Amsterdam, 1990, pp. 76–116.
18. R. E. Lynch and J. R. Rice, 'High accuracy finite difference approximations to solution of elliptic partial differential equations', *Proc. Nat. Acad. Sci.*, **75**, 2541–2544 (1978).
19. R. Boisvert, 'A fourth-order accurate fast direct method for the Helmholtz equation', in G. Binkhoff and A. Schoenstadt (eds), *Elliptic Problem Solvers II*, Academic, New York, 1984, pp. 35–44.
20. R. Bouard and M. Coutancea, 'The early stage development of the wake behind an impulsively started cylinder for $40 < Re < 10^4$', *J. Fluid Mech.*, **101**, 583–607 (1980).
21. Y. T. Chew, M. Cheng and S. C. Luo, 'A numerical study of flow past a rotating circular cylinder using a hybrid vortex scheme', *J., Fluid MEch.*, **299**, 35–71 (1995).

22. W. M. Collins and S. C. R. Dennis, 'Flow past an impulsively started circular cylinder', *J. Fluid Mech.*, **60**, 105–127 (1973).
23. P. A. Smith and P. K. Stansby, 'Impulsively started flow around a cylinder by the vortex method', *J. Fluid Mech.*, **194**, 45–77 (1988).
24. P. T. Ta, 'Numerical anlaysis of unsteady secondary vortices generated by an impulsively started circular cylinder', *J. Fluid Mech.*, **100**, 111–128 (1980).
25. M. Bar-Lev and H. T. Yang, 'Initial flow field over an impulsively started circular cylinder', *J. Fluid Mech.*, **72**, 625–647 (1975).
26. M. Tabata and S. Fujima, 'An upwind finite element scheme for high-Reynolds-number flows', *Int. j. numer. methods fluids*, **12**, 305–322 (1991).
27. A. Roshko, 'On the development of turbulent wakes from vortex sheets', *NACA Rep. 1191*, 1954.
28. H. M. Badr, M. Coutanceau, S. C. R. Dennis and C. Meneard, 'Unsteady flow past a rotating cylinder at Reynolds number 10^3 and 10^4', *J. Fluid Mech.*, **220**, 459–484 (1990).
29. A. Ongoren and D. Rockwell, 'Flow structure from an oscillating cylinder. Part 2. Mode competition in the near wake', *J. Fluid Mech.*, **191**, 225–245 (1988).
30. P. T. Tokumaru and P. E. Dimotakis, 'Rotary oscillation control of a cylinder wake', *J. Fluid Mech.*, **224**, 77–90 (1991).